In situ X-ray diffraction studies of the crystallization of $K_{0.5}Na_{0.5}NbO_3$ powders and thin films from an aqueous synthesis route

K. Bakken [a], N.H. Gaukås [a], O.G. Grendal [a], A.B. Blichfeld [a], S. Tominaka [b], K. Ohara [c], D. Chernyshov [d], J. Glaum [a], T. Grande [a], M.-A. Einarsrud [a,*]

[a] Department of Materials Science and Engineering, NTNU Norwegian University of Science and Technology, Trondheim, Norway
[b] International Center for Materials Nanoarchitectonics, National Institute for Materials Science, Ibaraki, Japan
[c] Diffraction and Scattering Division, Center for Synchrotron Radiation Research, Japan Synchrotron Radiation Research Institute, Hyogo, Japan
[d] Swiss-Norwegian Beamlines, European Synchrotron Radiation Facility, Grenoble, France

ARTICLE INFO

ABSTRACT

Aqueous chemical solution deposition is a promising route for ferroelectric $K_{0.5}Na_{0.5}NbO_3$ (KNN) thin films, requiring a stable precursor solution with complexed Nb^{5+}. Here, we report on the local structure of Nb-complexes forming during synthesis of KNN using Nb^{5+} complexed with either oxalic or malic acid. In situ total X-ray scattering during the decomposition, pyrolysis and crystallization of KNN precursor powders using the two routes revealed information of the changes in the atomic bond distances during the thermal processing, and a reaction scheme was presented. The structures of the Nb-complexes were proposed based on cluster modelling. In situ X-ray diffraction demonstrated the crystallization of KNN thin films from the precursor solutions, revealing how the complexing agents affect the formation of crystalline KNN films. The structure of the Nb-complexes was found to influence the kinetics of the combustion of the organic part of the deposited films, which further determined the crystallization temperature.

1. Introduction

Potassium sodium niobate, $K_{0.5}Na_{0.5}NbO_3$ (KNN), is one of the most promising and researched lead-free ferroelectric ceramic candidates due to the high piezoelectric coefficient and Curie temperature [1]. However, the properties of KNN are highly dependent on the processing as a wide range of values are generally reported for the material properties [1,2]. For device minimization, it is of general interest to use ferroelectric thin films preferably made by chemical solution deposition (CSD) as a simple, inexpensive and scalable industrial production route [3,4]. Moreover, CSD is flexible in terms of which precursors can be used and therefore also compositional range, resulting in chemically homogenous films. Aqueous CSD offers the possibility for a more environmentally friendly production [3,4]. However, a prerequisite for CSD is a stable precursor solution of the desired metal cations, which in case of niobium is challenging due to the low solubility of Nb in water [5].

The low solubility of niobium ionic species and affinity for oxygen ligands results in a strong tendency for polymerization to colloidal suspensions or precipitation. However, some soluble niobic oxide species exists, typically 6-coordinated hexaniobates, but their stability is highly dependent on the pH [5, 6]. Therefore, preparing an aqueous niobium solution is usually achieved by addition of complexing agents, such as the carboxylic acids; oxalic, malic, citric, lactic and glycolic acid [7]. Complexing niobium with oxalic acid in an aqueous solution result in a 7-coordinated Nb-complex containing 1–3 oxalate groups, dependent on the oxalic acid relative to Nb concentration and the pH [5]. For low oxalic acid concentrations (<0.4 M), the free oxalate ions break the Nb–O–Nb linkage and chelates Nb to form isolated Nb-oxalate complexes [5]. Several works report on the use of oxalate complexed Nb for production of KNN powders [8–11] and in a decomposition study of ammonium Nb-oxalate powder, the oxalate ligands were reported to start to decompose above 145 °C, resulting in $Nb_2O_5 \cdot H_2O$ at 330 °C [12]. Aqueous malic acid complexed niobium solutions has also been reported [7,11,13], although structural investigation of the malic acid Nb-complexes are not described in detail. However, an excess of malic acid relative to Nb was reported to be necessary for a stable aqueous solution [7]. Bayot et al. reported on various peroxo complexes of Nb, where a bidentate malic acid Nb-complex was presented, although with 3 peroxo groups [14].

Generally, non-aqueous CSD or sol-gel methods are most investigated for KNN films where the crystallization temperature ranges from 450 to 600 °C [15–19] dependent on the type of precursors and alkali excess. Aqueous CSD of KNN films has also been reported. Zhang et al. and Lu et al. prepared aqueous solutions where niobium was complexed with citric acid [20] or citric acid in combination with ethylene glycol and EDTA [21], resulting in polycrystalline KNN on Pt/Si substrates. An alkali nitrate-based synthesis route with oxalic or malic acid complexed niobium has recently been reported [11,22]. Gaukås et al. [11] prepared polycrystalline KNN films with columnar grains and (100) preferred orientation on (100) SrTiO$_3$ (STO). In films prepared by the oxalate complexed niobium solution, secondary phases were observed, while in the malic acid-based KNN, delayed decomposition and nucleation suppressed the formation of the secondary phases [11]. Pham et al. [22] prepared highly textured KNN films on STO using the oxalate complexed niobium precursor, with the addition of a salt flux (25 mol% excess KCl/NaCl). Films on (111) STO were found to be epitaxial, while on (100) and (110) STO an epitaxial layer was observed at the substrate interface, but the films were mainly polycrystalline [22]. Although KNN films from both oxalic and malic acid complexed precursor solutions have been prepared, the mechanisms behind the different crystallization paths, texture and secondary phase formation are unclear and call for further investigations.

Here, we report on the importance of the type of Nb-complex for the kinetics of the thermal decomposition and crystallization of KNN powders and thin films from aqueous solutions with oxalic and malic acid complexed niobium. *In situ* X-ray total scattering was used to investigate the choice of complexing agent on the thermal decomposition, while *in situ* X-ray diffraction was used to study the crystallization of KNN thin films from the same precursor solutions. The Nb-complex was found to govern the kinetics of the thermal decomposition from the initial Nb-complex, through formation of Nb-octahedra and to the final crystalline KNN nucleation, for both powders and thin films.

2. Experimental

2.1. Synthesis

The precursor solutions were prepared as described in Ref. [11]. For the oxalic acid-complexed solution, referred to as KNN-Ox, NH$_4$NbO(C$_2$O$_4$)$_2$·xH$_2$O (99.99%, Sigma-Aldrich, St. Louis, MO, USA) was dissolved in deionized water, and dried NaNO$_3$ (99%, Sigma-Aldrich, St. Louis, MO, USA) and KNO$_3$ (99%, Alfa Aesar, Haverhill, MA, USA) were added in a molar ratio of 1:0.525:0.525 (Nb:Na:K), giving 5 mol% excess of alkali metals. The concentration of the final solution was 0.25 M with respect to Nb, determined thermogravimetrically. In the malic acid-complexed solution, referred to as KNN-MA, a niobic acid precipitate was dissolved in distilled water with 0.33 M DL-malic acid (99%, Sigma-Aldrich, St. Louis, MO, USA) with a molar ratio of 1:2 (Nb:malic acid) before dried alkali nitrates were added in a ratio of 1:0.525:0.525 (Nb:Na:K), giving 5 mol% excess of alkali metals. The final solution had a Nb concentration of 0.14 M, determined thermogravimetrically. Precursor solutions with the addition of a salt flux (KNN-MAsf and KNN-Oxsf) were prepared by the addition of 15 mol% NaCl (99.95%, Merck, Darmstadt, Germany) and 15 mol% KCl (99.5%, Merck, Darmstadt, Germany) giving a total alkali excess of 30 mol%.

KNN precursor powders were prepared by drying the KNN-Ox and KNN-MA precursor solutions at 100 and 200 °C, respectively, for 24 h, followed by crushing in an agate mortar. One layer thick KNN precursor thin films were deposited on (100) STO single crystal (Crystal GmbH, Berlin, Germany) substrates, resulting in 23 nm and 17 nm thick films after crystallization for the KNN-Ox and KNN-MA films, respectively [11]. Prior to deposition, the substrates were rinsed with ethanol (96%) and the substrate surface was activated in an oxygen plasma cleaner (Femto, Diener Electronics, Ebhausen, Germany). The KNN precursor solutions were deposited onto the substrates using a spin coater

(WS–400B–6NPP-LITE/AS, Laurell Technologies, Montgomery, PA, USA) at 3500 rpm for 40 s, followed by drying on a hotplate at 200 °C for 3 min.

2.2. Characterization

In situ X-ray total scattering data for pair distribution function (PDF) analysis was collected at BL08W at SPring-8, Japan, in transmission mode using a 16 inch PerkinElmer XRD 1621 CN3 ES series flat panel detector [23] and a wavelength of $\lambda = 0.10713$ Å. Sample to detector distance (~53 cm) and geometry of setup was calibrated using a NIST CeO$_2$ standard. The dried precursor powders were filled in quartz capillaries (Ø2.0 mm from CharlesSupper Company, Westborough, USA). The ends of the capillaries were cut off to facilitate an airflow (0.03 L/min) through the capillary, with kaowool on both sides to avoid movement of the sample. The capillaries were heated with a heat blower (Leister LE Mini 800, Kaegiswil, Switzerland), controlled with a PID controller, up to 490 °C with a heating rate of ~0.15 °C/s. An empty capillary was used for background subtraction. All data were masked and integrated from 2D images to 1D diffractograms using pyFAI (v0.17.0) [24] and Jupyter Notebook (version 5.7.8). Background subtraction and conversion to PDF was done using PDFgetX3 (v2.0.0) [25] and Jupyter Notebook with a Q$_{max}$ of 17.5 Å^{-1}. The Nb-clusters were build using Chem3D (v19.1) and adopted from Nb-complexes reported in literature, where the atomic distances were adjusted to fit the experimental data. The PDFs for the Nb-clusters were calculated using the DiffPy python package (v3.0) [26]. Rietveld refinement was performed on selected diffraction patterns, see Supplementary Information for details.

Synchrotron X-ray diffraction (XRD) on the thin films was conducted at the BM01 end-station, Swiss-Norwegian Beamlines (SNBL) at ESRF (The European Synchrotron Radiation Facility, Grenoble, France). The films were characterized at two different experimental sessions using wavelengths of 0.78449 Å and 0.77624 Å, which was chosen to suppress fluorescence of Sr from the STO substrates. A Pilatus2M 2D-detector was used [27] and the films were heated *in situ* on a set up described in detail by Blichfeld et al. [28] The experimental details and the procedure for data treatment are outlined in Blichfeld et al. [28] and Bakken et al. [29] In short, the films were placed on top of a heating plate and aligned so the beam footprint was centred on the film. During the heating, the film was measured in grazing incidence and to compensate for thermal expansion of the setup, data was recoded sequentially at different heights. The signal from the substrate and thermal expansion data were combined to calculate the real sample to detector distance for each measurement height, and the data was corrected based on this calibration. The preliminary data processing and inspection of the powder diffraction profiles were done with BM01 software tools, BUBBLE [27] and MEDVED [30]. The final data processing was done in Jupyter Notebook utilizing the pyFAI package (see Blichfeld et al. [28] for more details) accounting for corrections and calibrations specific for the given *in situ* setup. Batch Rietveld refinements were performed using MAUD software (Materials Analysis Using Diffraction v2.78) [31], where the pseudo-cubic lattice parameter was the only refined parameter.

3. Results

3.1. In situ X-ray total scattering of the decomposition of KNN precursor powders

The *in situ* X-ray total scattering from the KNN-Ox and KNN-MA precursor powders is shown in Fig. 1(a) and (b), respectively. The total scattering shows that crystallization of KNN started at 348 °C for KNN-Ox and at 387 °C for KNN-MA. In addition to KNN, the secondary phase K$_4$Nb$_6$O$_{17}$ nucleated at 350 and 402 °C for KNN-Ox and KNN-MA, respectively, and this phase remained in the powders, even after annealing at 490 °C for 20 min. From Rietveld refinements, there were equal amounts of KNN and secondary phase in KNN-Ox when nucleation
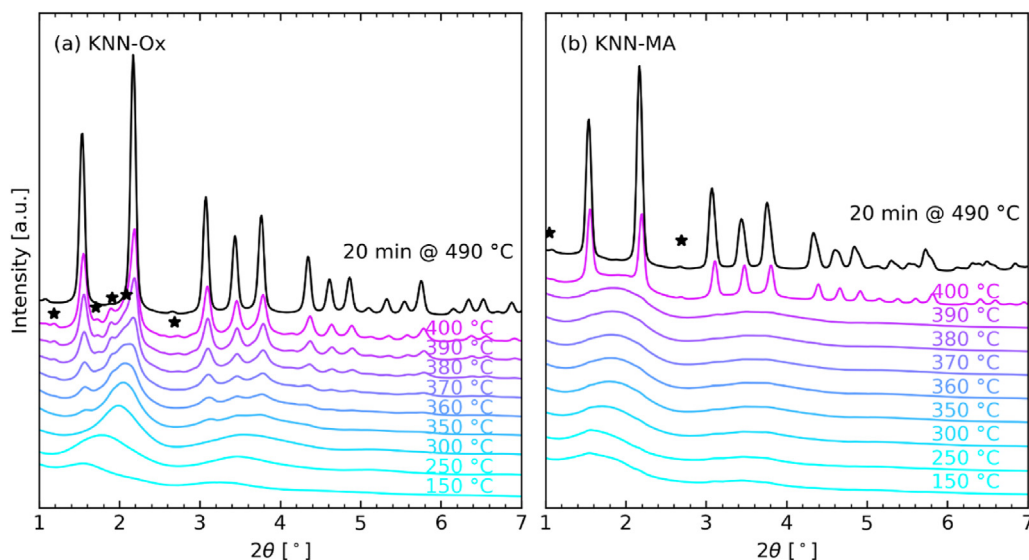
Fig. 1. X-ray total scattering for (a) KNN-Ox and (b) KNN-MA precursor powders during *in situ* annealing. Peaks corresponding to the $K_4Nb_6O_{17}$ secondary phase are marked with stars.

occurred. The amount of secondary phase steadily decreased to 6.3 wt% during the heating and annealing step, but even after cooling 2.8 wt% $K_4Nb_6O_{17}$ remained in the powder. However, in the KNN-MA precursor, the amount of $K_4Nb_6O_{17}$ was observed to be 18.8 wt% right after nucleation, decreasing to 2.4 wt% during the annealing at 490 °C and 1.7 wt% after cooling. The lattice parameters of the final KNN powders were in the same range (Table S1 in Supplementary Information), demonstrating that the type of precursor does not significantly alter the final crystalline KNN phase in the powders.

The different trends in the total scattering data as a function of temperature demonstrate a difference in nucleation behaviour, related to the Nb-complexes forming in the precursor solutions, which has also previously been reported by infrared (IR) spectra and thermogravimetric (TG) analysis [11]. PDFs of the KNN-Ox and KNN-MA precursor powders at 150 °C are presented in Fig. 2. The temperature was chosen as limited thermal decomposition has occurred, so the PDFs and indicated structures should be representative for the structure of the initial Nb-complexes. Schematics of the modelled Nb-clusters are displayed and

the calculated PDFs from these clusters are provided. 3D images of the Nb-clusters are given in Figure S2 in the Supplementary Information. The oxalate cluster (Fig. 2(a)) was taken from Ref. [5], and the calculated PDF demonstrates that this Nb-cluster exhibits the major peaks from the refined data; Nb=O distance at 1.75 Å, Nb–O distance at 2.15 Å, Nb–C distance at 2.96 Å and the closest Nb–Nb distance at 3.77 Å. However, the relative intensities and widths of the peaks are not featured in the calculated PDF from the cluster model, as there is likely an array of Nb-clusters in the KNN-Ox precursor powder in addition to other organic species. Likewise, for the calculated PDF of the modelled Nb-cluster of the KNN-MA precursor (Fig. 2(b), based on the work reported in Ref. [14]), the model incorporates the major peaks of the measured data; Nb–O distance at 2.16 Å, Nb–C distance at 2.98 Å and the closest Nb–Nb distance at 3.78 Å. Moreover, the peak width in the PDFs is an important distinction between the two precursor powders. The peaks in the experimental PDFs of KNN-Ox precursor powder (Fig. 2(a)) are sharper than for the KNN-MA precursor (Fig. 2(b)), indicating more homogenous Nb-complexes, while in the KNN-MA precursor there is likely an
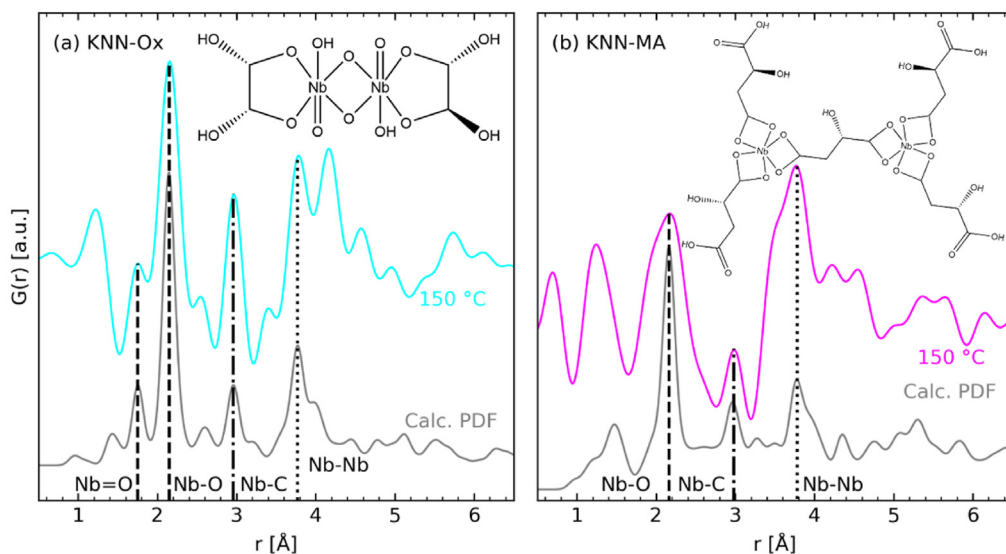

Fig. 2. PDFs for (a) KNN-Ox and (b) KNN-MA precursor powders from the initial part of the *in situ* annealing. Calculated PDFs from the illustrated Nb-clusters are shown and the most significant Nb-bonds are indicated.

assortment of Nb-complexes, but with the same Nb–O configurations.

Fig. 3 shows the converted PDFs for the KNN-Ox and KNN-MA precursor powders as a function of temperature during the annealing. In the case of the KNN-Ox precursor powder (Fig. 3(a)), the PDF change with increasing temperature from 150 °C. The decomposition is demonstrated by the decrease in intensity of the Nb–C peak with increasing temperature. With further heating, the Nb–O distance shifts towards the distance for crystalline KNN, while simultaneously the intensity of the peak associated with the closest Nb–Nb distance in corner-sharing octahedra (cso) increases and alkali is incorporated gradually into the structure (seen from the emerging Nb–A peak, where A denotes alkali). However, the Nb–Nb distance shifts abruptly to correspond to the value for the lattice constant after crystallization occurred at 348 °C. This is consistent with previously reported IR spectra, where bands corresponding to perovskite-like species were present in the temperature range 200–300 °C [11]. TG analysis of the same powders demonstrated that the majority of the mass loss occurred in the same temperature range [11]. The decomposition of the KNN-MA precursor was more gradual according to the converted PDFs (Fig. 3(b)). With increasing temperature, the peak from the Nb–Nb distance in corner-sharing octahedra gradually becomes more intense, while the broad peak corresponding to the Nb–O distance gradually splits into a peak with the distance observed in crystalline KNN and a shoulder (marked with * in Fig. 3(b)). The shoulder of the Nb–O peak is present in the PDF of the crystalline KNN-MA powder, but after annealing at 490 °C for 20 min, it had faded (not shown). This shoulder likely corresponds to a deviating Nb–O distance in the un-decomposed organic residue. As observed for the KNN-Ox precursor, there is an abrupt shift in the Nb–Nb distance to a value corresponding to the lattice constant after crystallization also in the KNN-MA powder, but the incorporation of alkali into the structure was continuous. The peak position and the assigned atomic pairs found in both crystalline KNN powders are listed in Table 1 and compare well with literature values [32]. Apparent peaks in the PDFs below ~1 Å are artefacts of the conversion and does not represent any real atomic pair distances.

Table 1
The assigned atomic pair to the peak positions observed in the crystalline KNN powders after annealing at 490 °C for 20 min. A denotes alkali (K, Na).

Powder	Peak position [Å]	Assigned atomic pair
KNN-Ox	1.95	Nb–O
	2.78	A-O
	3.46	Nb–A
	3.99	a (Nb–Nb, A-A, O–O)
KNN-MA	1.96	Nb–O
	2.79	A-O
	3.46	Nb–A
	3.99	a (Nb–Nb, A-A, O–O)

3.2. Crystallization of KNN thin films

The *in situ* XRD patterns of KNN-Ox and KNN-MA thin films during annealing of as-deposited precursor films as they crystallize are shown in Fig. 4. In general, the thin films follow the same phase evolution and crystallization behaviour as reported for the corresponding powders during *in situ* X-ray total scattering (Section 3.1) and *ex situ* results reported for powders and thin films from the same precursor solutions [11]. However, the temperatures are shifted due to the different processing conditions in the capillaries compared to the thin films. The KNN-Ox film (Fig. 4(a)) crystallize at 450 °C, but there is also formation of the secondary $K_4Nb_6O_{17}$ phase (seen as a series of sharp peaks in the 2θ-range 5.3–6.7°, marked with stars). The secondary phase is present in the KNN-Ox film from 490 to 582 °C, but the peak intensity decreases rapidly as the temperature increases. The KNN-MA thin film (Fig. 4(b)) crystallizes at 517 °C, without formation of any secondary phases. The grey shaded region in the XRD patterns are areas where there is no diffraction recorded due to the gaps in the detectors. The peaks present at temperatures before KNN crystallization, which is indicated by the appearance of the (100) diffraction line, are due to diffuse scattering from the single crystal STO substrates, which could not be masked.
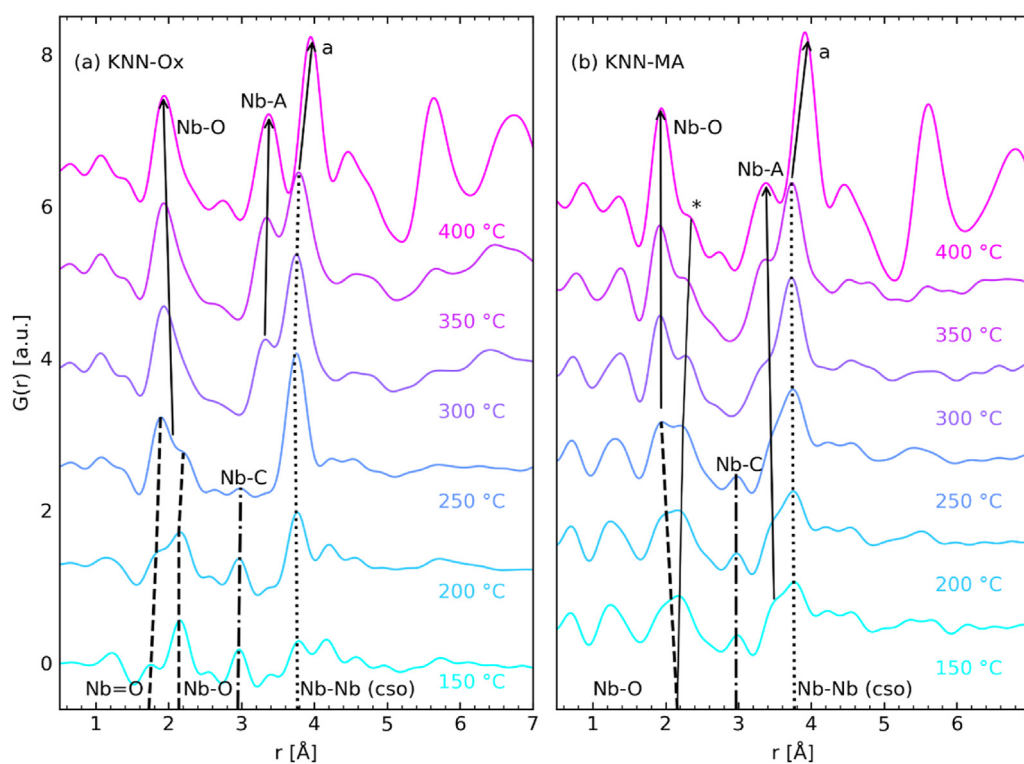
Fig. 3. PDFs of (a) KNN-Ox and (b) KNN-MA precursor powders during annealing. The main peaks in the PDFs are indicated, showing how the most important Nb distances develop during decomposition of the precursor. The distance corresponding to the lattice parameter is denoted "a" and "A" refers to alkali (K and Na). The emerging shoulder corresponding to a Nb–O distance in the organic residue phase is marked with an asterisk.
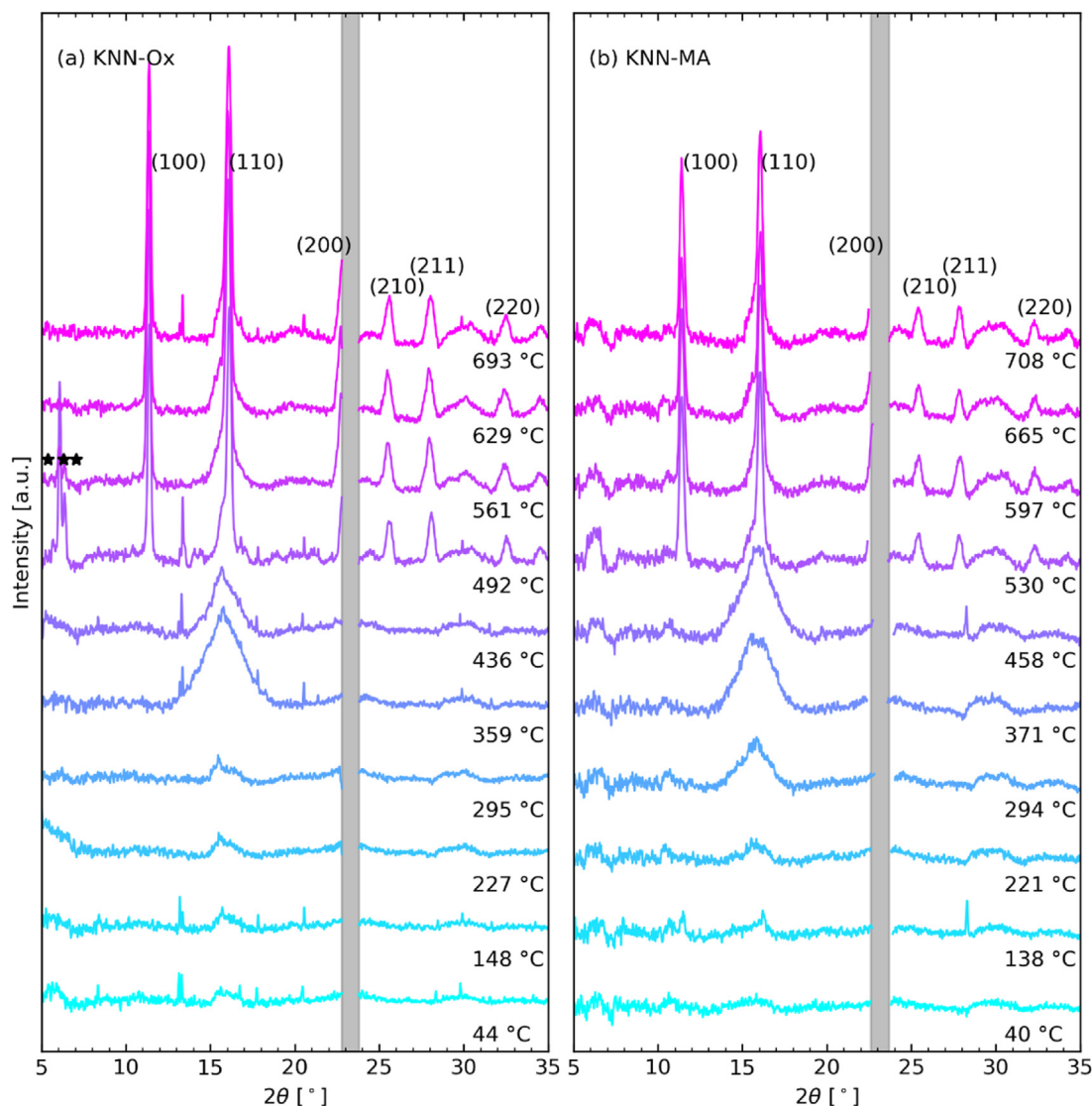
Fig. 4. *In situ* XRD patterns for (a) KNN-Ox and (b) KNN-MA thin films during annealing. The grey shaded regions are areas without any recorded data due to gaps in the detector. Peaks from $K_4Nb_6O_{17}$ are marked with stars. Peaks appearing before crystallization of KNN (seen as the first appearance of the KNN (001) peak) are due to diffuse scattering of the substrate that could not be masked. The heating rate was 0.2 °C/s for both samples and the wavelengths were 0.78449 Å and 0.77624 Å, respectively.

The KNN-MA thin film has a more intense central reflection on the (100) diffraction line compared to the KNN-Ox films, as seen from the normalized azimuthal plot in Fig. 5. This increased intensity in the centre indicates a degree of preferred (100) orientation in the film or a thin epitaxial layer at the substrate interface, as reported previously [10]. However, the intensity difference is low compared to what has been reported for textured single layer $BaTiO_3$ thin films on STO [29], so the degree of preferred orientation was modest for the KNN films.

The nucleation temperature and temperature range for the presence of the secondary $K_4Nb_6O_{17}$ phase are shown in Fig. 6(a) as a function of heating rate. The KNN-Ox films in general have a lower nucleation temperature compared to KNN-MA, independent of the heating rate used
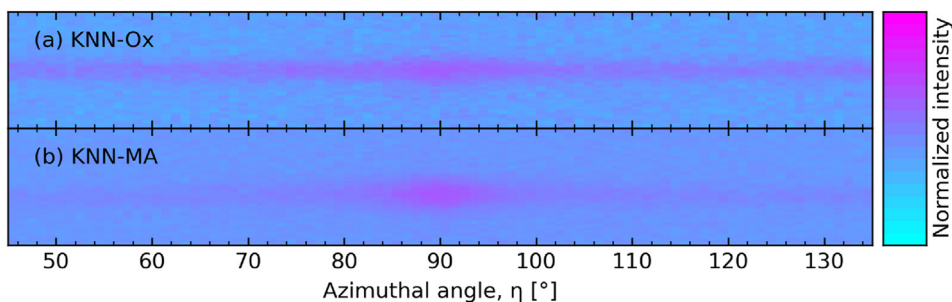
Fig. 5. Normalized azimuthal intensity distribution of the (100) diffraction line for crystalline (a) KNN-Ox and (b) KNN-MA thin films, recorded at ambient temperature. Both films were heated with 0.2 °C/s to 700 °C and held for 20–30 min at the maximum temperature.
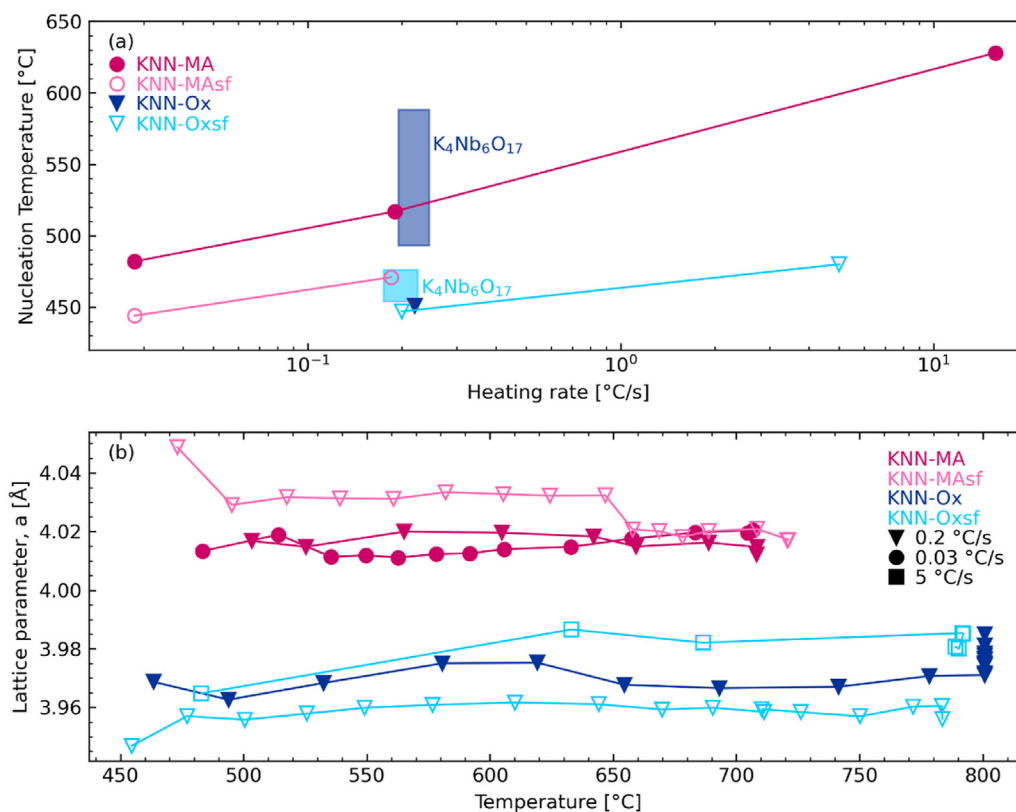
Fig. 6. (a) Nucleation temperature and temperature window for the presence of the $K_4Nb_6O_{17}$ secondary phase versus heating rate for *in situ* annealing of KNN-Ox and KNN-MA thin films. (b) Pseudo-cubic lattice parameter from Rietveld refinements as a function of temperature during *in situ* annealing of KNN-Ox and KNN-MA thin films.

during the annealing. Moreover, the nucleation temperatures generally increase with faster heating rate. The addition of salt flux has been reported to aid texture formation in KNN thin films [22]. While no improvement of the degree of texture was observed in the *in situ* crystallization of single layered thin films in this work, the salt flux does lower the nucleation temperatures and destabilizes the secondary phase such that phase pure KNN is achieved at lower temperatures. The pseudo-cubic lattice parameters of the KNN thin films as a function of temperature during annealing are shown in Fig. 6(b). In general, the KNN-MA films have a larger lattice parameter than the KNN-Ox films. The lattice parameter in the latter also exhibit a slight increase with temperature during the annealing.

4. Discussion

4.1. Influence of the Nb-complexing agent on the formation of KNN

The different decomposition and crystallization behaviour observed for KNN powders and thin films originate from the different chemistry of the Nb-complexes in the precursor solutions. These Nb oxalic or malic acid complexes govern the thermodynamics and kinetics of the KNN crystallization, schematically illustrated in Fig. 7. Although the character of the initial Nb-complexes and the removal of the organic part differ, the later stages of the KNN formation are the same for both routes, as the same atomic pair distances are observed from the PDFs (Fig. 3). After formation of Nb-octahedra with alkali counter ions, the octahedra form corner-sharing networks, which incorporate charge compensating alkali cations, until enough alkali cations are included and crystallization of KNN occurs. However, the kinetics of this process depends on the initial Nb-complex. For the oxalate complexed Nb (KNN-Ox), the clusters are small, but there is a low energy barrier for polymerization and octahedral formation due to uniform clusters. This means that the Nb-octahedra

form at low temperatures, which gives low nucleation barriers for crystallization of the perovskite, but also secondary phases such as $K_4Nb_6O_{17}$. Although the energy barrier for crystallization is low for KNN-Ox, the crystallization kinetics is slow due to modest thermal energy, hence the overall transformation rate is low. The crystallinity of the KNN-Ox powder continues to increase over a wider temperature window, as seen from the total scattering data in Fig. 1(a). In the malate complexed Nb system (KNN-MA) a greater distribution of different configurations for the Nb-complexes are present, and organic chains are "locked" into the structure, giving a gradual transformation from the initial clusters to Nb–O octahedra. In this system a higher temperature is also needed before the octahedra form corner-sharing networks with alkali incorporation. However, once nucleation is favourable, the KNN-MA system quickly crystallizes and achieves the final crystallinity (Fig. 1) due to sufficient thermal energy. Although the Nb-complexing agents affect the kinetics of the KNN crystallization, both routes result in the same degree of crystallinity and crystal structure after annealing, provided the annealing temperature is greater than the respective nucleation temperatures.

This proposed reaction scheme is consistent with previously published results on the same precursor solutions [11]. In this work, the IR spectra showed broad bands indicating Nb–O octahedra above 300 °C in the KNN-Ox powders, while in the KNN-MA powders the same band appeared only at 400 °C, demonstrating slower reaction kinetics for the KNN-MA precursor decomposition. TG analysis of the same powders revealed that in the KNN-Ox powder, the mass loss associated with the removal of organics occurs in the temperature range 250–350 °C, while for KNN-MA there is a two-step decrease in mass and the mass loss continuous until 500–550 °C [11]. Taking into account the different measurement conditions, these temperatures correspond well with those observed by *in situ* X-ray total scattering in this work.
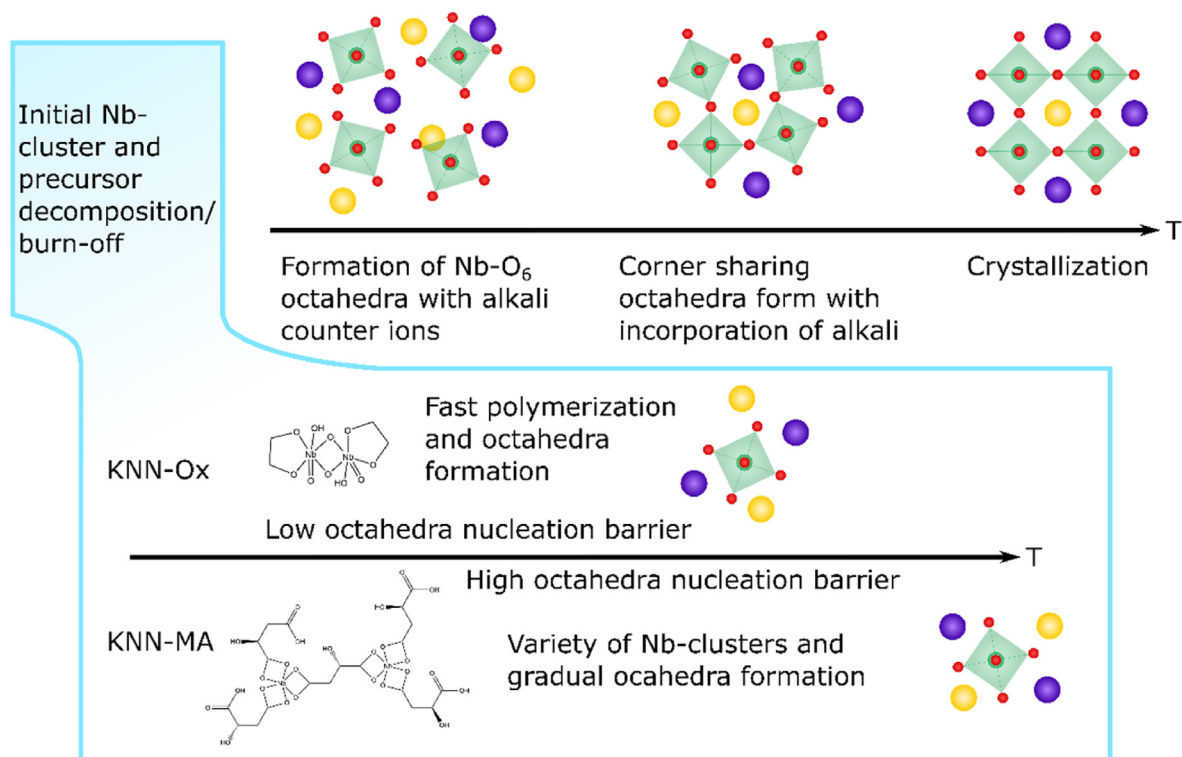
Fig. 7. Illustration of the crystallization process for KNN from different precursor solutions as a function of temperature (T). The fundamental difference between the oxalate- and malic acid-complexed solutions are related to the decomposition of the initial Nb-clusters resulting from the two different complexing agents.

4.2. Factors affecting crystallization of KNN thin films

The KNN thin films from oxalate and malic acid complexed Nb precursor solutions follow the same reaction scheme as illustrated in Fig. 7. The KNN-Ox films crystallize at a lower temperature than the KNN-MA films. Formation of the secondary $K_4Nb_6O_{17}$ phase occurs in both systems, in line with the powder results reported in this work and previously published results on KNN thin films from the same precursor solutions [11,22]. However, in the powders, the resulting crystalline KNN phase have similar lattice parameters after annealing. This is not the case for the thin films, as the KNN-Ox films have a significantly lower lattice parameter than the KNN-MA films. The difference in lattice parameters demonstrate that structurally different KNN forms dependent on the precursor solution, which could influence the functional properties of the films. The lattice parameter of the KNN-Ox films also increases with temperature during annealing, while the KNN-MA films does not change significantly with temperature. A possible explanation is heterogeneous but randomly oriented in-plane strained nucleation at the substrate for the KNN-Ox films followed by relaxation during annealing, while the KNN-MA nucleation is homogeneous. Such a nucleation scheme would explain the larger lattice parameters observed for KNN-MA than the KNN-Ox films. Compositional differences are also an alternative explanation, however as this is not observed in the powders or by previous results [11,22], it seems more likely that the difference in the lattice parameter is related to the nucleation behaviour.

Different heating rates were investigated for the annealing of the thin films as this is expected to influence the nucleation and degree of preferential orientation in the films. However, no significant degree of preferred orientation was observed for any of the KNN thin films, independent of heating rate and precursor solution. Only the nucleation temperature was affected, as seen from Fig. 6(a), which is expected from kinetic considerations. Addition of salt flux to the precursor solutions gave no improved texture during annealing of single layered KNN thin films, but it did lower the nucleation temperature for the KNN-MA films and reduced the temperature range for the presence of secondary phases

in the KNN-Ox films. These observations support the proposed effect of the salt flux outlined in Pham et al., where the salt flux forms a eutectic melt from which alkali species are stabilized and the melt facilitates KNN precipitation at lower temperatures [22].

Textured and epitaxial multilayered KNN films on STO substrates have been reported from the same oxalic and malic acid complexed aqueous precursor solutions [11,22]. However, in this work only modest (100) preferred orientation was observed for the single layered KNN-MA thin films (Fig. 5). The texture earlier observed in multilayer KNN films [11,22] is likely induced by the repeated annealing process used for fabricating the films by multible depositions. With repeated annealing cycles, reorientation of the already crystalline layers could occur. The reoriented layers will then act as seed layers for the consecutive deposited layers, resulting in texture in the multilayer KNN films. The addition of salt flux could enhance this reorientation effect, explaining the increase in texture reported [22]. However, this effect would not be observed for a single crystallized layer.

5. Conclusion

KNN powders and thin films from an aqueous synthesis route were characterized by *in situ* X-ray total scattering and X-ray diffraction, respectively. The *in situ* analysis revealed that the choice of Nb complexing agent determines the kinetics of the precursor decomposition and the nucleation behaviour of the thin films and therefore also the resulting lattice parameters. Oxalate complexed Nb was observed to give a low nucleation barrier toward Nb–O octahedra formation, resulting in a low crystallization temperature for both KNN and the secondary phase $K_4Nb_6O_{17}$. Complexing Nb with malic acid delayed the crystallization, which inhibited formation of secondary phases as the nucleation kinetics were faster at higher temperature. In the thin films, the KNN-Ox films exhibited smaller lattice parameters than the KNN-MA films as a result of different nucleation behaviour. No significant degree of texture was observed in the single layered KNN films, independent of precursor solution, salt flux and heating rate.

Declaration of interests

Acknowledgment

Appendix A. Supplementary data

Supplementary data to this article can be found online at https ://doi.org/10.1016/j.oceram.2021.100147.

References

[1] J.-F. Li, K. Wang, F.-Y. Zhu, L.-Q. Cheng, F.-Z. Yao, (K, Na)NbO3-based lead-free piezoceramics: fundamental aspects, processing Technologies, and remaining challenges, J. Am. Ceram. Soc. 96 (12) (2013) 3677–3696, https://doi.org/10.1111/jace.12715.

[2] J. Wu, D. Xiao, J. Zhu, Potassium–sodium niobate lead-free piezoelectric materials: past, present, and future of phase boundaries, Chem. Rev. 115 (7) (2015) 2559–2595, https://doi.org/10.1021/cr5006809.

[3] R.W. Schwartz, T. Schneller, R. Waser, Chemical solution deposition of electronic oxide films, C R Chim 7 (5) (2004) 433–461, https://doi.org/10.1016/j.crci.2004.01.007.

[4] N. Bassiri-Gharb, Y. Bastani, A. Bernal, Chemical solution growth of ferroelectric oxide thin films and nanostructures, Chem. Soc. Rev. 43 (7) (2014) 2125–2140, https://doi.org/10.1039/c3cs60250h.

[5] J.-M. Jehng, I.E. Wachs, Niobium oxide solution chemistry, J. Raman Spectrosc. 22 (2) (1991) 83–89, https://doi.org/10.1002/jrs.1250220207.

[6] D. Fast, M. Clark, L. Fullmer, K. Grove, M. Nyman, B. Gibbons, M. Dolgos, Using simple aqueous precursors for a green synthetic pathway to potassium sodium niobate thin films, Thin Solid Films 710 (2020) 138270, https://doi.org/10.1016/j.tsf.2020.138270.

[7] F. Fairbrother, J.B. Taylor, Water-soluble complexes of niobium (columbium) and tantalum. Part I. Complexes with α-hydroxy-acids and (2-hydroxyethyl)-amines, J. Chem. Soc. (1956) 4946–4954, https://doi.org/10.1039/JR9560004946, 961.

[8] A.B. Haugen, F. Madaro, L.-P. Bjørkeng, T. Grande, M.-A. Einarsrud, Sintering of sub-micron K0.5Na0.5NbO3 powders fabricated by spray pyrolysis, J. Eur. Ceram. Soc. 35 (5) (2015) 1449–1457, https://doi.org/10.1016/j.jeurceramsoc.2014.11.011.

[9] D.-Q. Zhang, Z.-C. Qin, X.-Y. Yang, H.-B. Zhu, M.-S. Cao, Study on synthesis and evolution of sodium potassium niobate ceramic powders by an oxalic acid-based sol–gel method, J. Sol. Gel Sci. Technol. 57 (1) (2011) 31–35, https://doi.org/10.1007/s10971-010-2320-8.

[10] H. Khorrami G, A. Kompany, A. Khorsand Zak, Structural and optical properties of (K,Na)NbO3 nanoparticles synthesized by a modified sol–gel method using starch media, Adv. Powder Technol. 26 (1) (2015) 113–118, https://doi.org/10.1016/j.apt.2014.08.013.

[11] N.H. Gaukås, S.M. Dale, T.M. Ræder, A. Toresen, R. Holmestad, J. Glaum, M.-A. Einarsrud, T. Grande, Controlling phase purity and texture of K0.5Na0.5NbO3 thin films by aqueous chemical solution deposition, Materials 12 (13) (2019) 2042.

[12] T.T. Su, Y.C. Zhai, H. Jiang, H. Gong, Studies on the thermal decomposition kinetics and mechanism of ammonium niobium oxalate, J. Therm. Anal. Calorim. 98 (2) (2009) 449, https://doi.org/10.1007/s10973-009-0300-4.

[13] E.R. Camargo, M. Popa, M. Kakihana, Sodium niobate (NaNbO3) powders synthesized by a wet-chemical method using a water-soluble malic acid complex, Chem. Mater. 14 (5) (2002) 2365–2368, https://doi.org/10.1021/cm011696d.

[14] D. Bayot, M. Devillers, Peroxo complexes of niobium(V) and tantalum(V), Coord. Chem. Rev. 250 (19) (2006) 2610–2626, https://doi.org/10.1016/j.ccr.2006.04.011.

[15] X. Wu, L. Wang, W. Ren, X. Yan, P. Shi, X. Chen, X. Yao, Preparation and properties of (110) oriented lead-free sodium potassium niobate thin films by MOD method, Ferroelectrics 367 (1) (2008) 61–66, https://doi.org/10.1080/00150190802365947.

[16] A. Chowdhury, J. Bould, M.G.S. Londesborough, S.J. Milne, Fundamental issues in the synthesis of ferroelectric Na0.5K0.5NbO3 thin films by Sol–Gel processing, Chem. Mater. 22 (13) (2010) 3862–3874, https://doi.org/10.1021/cm903697j.

[17] C. Kang, J.-H. Park, D. Shen, H. Ahn, M. Park, D.-J. Kim, Growth and characterization of (K0.5 Na0.5)NbO3 thin films by a sol–gel method, J. Sol. Gel Sci. Technol. 58 (1) (2011) 85–90, https://doi.org/10.1007/s10971-010-2359-6.

[18] W. Zhang, H.Y. Zhu, X.H. Zhang, H. Wu, J.Q. Bao, F.R. Hu, Structural and electrical study of highly (100)-oriented KNN films fabricated by a sol-gel non-alkoxide process, Ceram. Int. 45 (17) (2019) 22156–22162, https://doi.org/10.1016/j.ceramint.2019.07.234.

[19] Q. Yu, J.-F. Li, Y. Chen, L.-Q. Cheng, W. Sun, Z. Zhou, Z. Wang, Effect of pyrolysis temperature on sol–gel synthesis of lead-free piezoelectric (K,Na)NbO3 films on Nb: SrTiO3 substrates, J. Am. Ceram. Soc. 97 (1) (2014) 107–113, https://doi.org/10.1111/jace.12675.

[20] D. Zhang, F. Zheng, X. Yang, L. Feng, X. Huang, H. Liu, M. Cao, Preparation and ferroelectric properties of K0.5Na0.5NbO3 thin films derived from non-alcohol niobium salt sol-gel process, Integrated Ferroelectrics Int. J. 154 (1) (2014) 97–102, https://doi.org/10.1080/10584587.2014.904166.

[21] T. Lu, K. Zhu, J. Liu, J. Wang, J. Qiu, Lead-free (K, Na)NbO3 thin films derived from chemical solution deposition modified with EDTA, J. Mater. Sci. Mater. Electron. 25 (2) (2014) 1112–1116, https://doi.org/10.1007/s10854-013-1696-y.

[22] K.-N. Pham, N.H. Gaukås, M. Morozov, T. Tybell, P.E. Vullum, T. Grande, M.-A. Einarsrud, Epitaxial K0.5Na0.5NbO3 thin films by aqueous chemical solution deposition, Royal Society Open Science 6 (1) (2019) 180989, https://doi.org/10.1098/rsos.180989.

[23] K. Ohara, S. Tominaka, H. Yamada, M. Takahashi, H. Yamaguchi, F. Utsuno, T. Umeki, A. Yao, K. Nakada, M. Takemoto, S. Hiroi, N. Tsuji, T. Wakihara, Time-resolved pair distribution function analysis of disordered materials on beamlines BL04B2 and BL08W at SPring-8, J. Synchrotron Radiat. 25 (6) (2018) 1627–1633, https://doi.org/10.1107/S1600577518011232.

[24] G. Ashiotis, A. Deschildre, Z. Nawaz, J.P. Wright, D. Karkoulis, F.E. Picca, J. Kieffer, The fast azimuthal integration Python library: pyFAI, J. Appl. Crystallogr. 48 (Pt 2) (2015) 510–519, https://doi.org/10.1107/s1600576715004306.

[25] P. Juhas, T. Davis, C.L. Farrow, S.J.L. Billinge, PDFgetX3: a rapid and highly automatable program for processing powder diffraction data into total scattering pair distribution functions, J. Appl. Crystallogr. 46 (2) (2013) 560–566, https://doi.org/10.1107/S0021889813005190.

[26] C.L. Farrow, P. Juhas, J.W. Liu, D. Bryndin, E.S. Božin, J. Bloch, T. Proffen, S.J. Billinge, PDFfit2 and PDFgui: computer programs for studying nanostructure in crystals, J. Phys. Condens. Matter 19 (33) (2007) 335219, https://doi.org/10.1088/0953-8984/19/33/335219.

[27] V. Dyadkin, P. Pattison, V. Dmitriev, D. Chernyshov, A new multipurpose diffractometer PILATUS@SNBL, J. Synchrotron Radiat. 23 (2016) 825–829, https://doi.org/10.1107/s1600577516002411.

[28] A.B. Blichfeld, K. Bakken, D. Chernyshov, J. Glaum, T. Grande, M.-A. Einarsrud, Experimental setup for high-temperature in situ studies of crystallization of thin films with atmosphere control, J. Synchrotron Radiat. 27 (5) (2020) 1209–1217, https://doi.org/10.1107/S1600577520010140.

[29] K. Bakken, A.B. Blichfeld, D. Chernyshov, T. Grande, J. Glaum, M.-A. Einarsrud, Mechanisms for texture in BaTiO3 thin films from aqueous chemical solution deposition, J. Sol. Gel Sci. Technol. 95 (3) (2020) 562–572, https://doi.org/10.1007/s10971-020-05356-2.

[30] D. Chernyshov, V. Dyadkin, W. van Beek, A. Urakawa, Frequency analysis for modulation-enhanced powder diffraction, Acta Crystallogr. A 72 (4) (2016) 500–506, https://doi.org/10.1107/S2053273316008378.

[31] L. Lutterotti, Total pattern fitting for the combined size–strain–stress–texture determination in thin film diffraction, Nucl. Instrum. Methods Phys. Res. Sect. B Beam Interact. Mater. Atoms 268 (3) (2010) 334–340, https://doi.org/10.1016/j.nimb.2009.09.053.

[32] S. Gupta, V. Petkov, S. Priya, Local atomic structure of KxNa(1−x)NbO3 by total x-ray diffraction, Appl. Phys. Lett. 105 (23) (2014) 232902, https://doi.org/10.1063/1.4903512.